Trabajo Fin de Máster

Máster en Física

Unveiling the Optical Properties of InP/InGaP Nanowires using Spectroscopic Characterization Techniques

(Revelando las Propiedades Ópticas de Nanohilos de InP/InGaP a través de Técnicas de Caracterización Espectroscópica)

Autor: Vanessa Giselle Hinojosa Chasiquiza

Tutor/es: Dr. Jorge Serrano

Prof. Juan Jiménez

Valladolid, Spain, July 15, 2022

Resumen

Los nanohilos semiconductores son materiales prometedores para la próxima generación de células solares tándem. Su dimensión permite combinar una gran variedad de materiales no permitidos en las células solares planas debido a la gran diferencia en los parámetros de red. Los nanohilos también han mostrado un gran potencial en aplicaciones eléctricas, biomédicas, fotónicas y otras. Se han utilizado diferentes configuraciones, dopaje y concentraciones. Por lo tanto, comprender las propiedades de los nanohilos es crucial para desarrollar nanohilos para diferentes aplicaciones. En ese contexto, las técnicas ópticas son herramientas no invasivas muy poderosas para caracterizar nanohilos semiconductores. En este trabajo, hemos caracterizado nanohilos InP/InGaP axialmente heteroestructurados con espectroscopia micro-Raman, micro-fotoluminiscencia, espectroscopia Raman mejorada con la punta (TERS), fotoluminiscencia mejorada con la punta (TEPL) y análisis de rayos X de dispersión de energía. Encontramos asombrosos fenómenos ópticos en los nanohilos de InP/InGaP investigados, que consisten en dos uniones p-n hechas de InP y InGaP y conectadas axialmente mediante un diodo túnel formado por n^+-InP/p^+-InGaP. En particular, hallamos una resonancia local en el espectro RAman correspondiente a la union túnel acompañada por la ruptura de las reglas de selección Raman. Además, se observó un modo amortiguado de plasmón en el lado fuertemente dopado de tipo p de la unión túnel. Las mediciones de fotoluminiscencia permitieron detectar la presencia de una capa de InGaP parásita que creció lateralmente en la parte inferior del nanohilo.

Palabras clave: Micro Raman, micro fotoluminiscencia, nanohilos axialmente heteroestructurados, espectroscopía Raman de punta mejorada (TERS), fotoluminiscencia de punta mejorada (TEPL), modos acoplados de plasmón-fonón LO (LOPC)

Abstract

Semiconductor nanowires are promising materials for the next generation of tandem solar cells. Its dimension allows one to combine a large variety of materials not allowed in planar solar cells because of the large lattice mismatch. Nanowires have also shown great potential in electrical, biomedical, photonics, and other applications. Different configurations, doping, and concentrations have been used. Therefore, understanding the nanowire properties is crucial to grow nanowires for different applications. In that context, optical techniques are very powerful non-invasive tools for characterizing semiconductor nanowires. In this work, we have characterized axially hetero-structured InP/InGaP nanowires with micro-Raman spectroscopy, micro-photoluminescence, tip-enhanced Raman spectroscopy, tip-enhanced photoluminescence, and energy-dispersive X-ray analysis. We found peculiar optical phenomena along the nanowire, which consists of two p n junctions made of InP and InGaP, respectively, axially bridged by a n^+-InP/p^+-InGaP tunnel diode. In particular, a local resonance at the tunnel junction is accompanied by the breakdown of the Raman selection rules. Furthermore, plasmon damped mode was observed in the heavily p-type doped side of the tunnel junction. Photoluminescence measurements allowed to detect the presence of a parasitic InGaP layer grown laterally at the bottom of the nanowire.

Keywords: Raman, photoluminescence, axially hetero-structured nanowires (NWs), tip-enhanced Raman Spectroscopy (TERS), tip-enhanced photoluminescence Spectroscopy (TEPL), LO phonon plasmon coupled (LOPC) modes, tandem solar cells, tunnel junction

Contents

List of Figures

List of Tables

List of Presentations

[1] Hinojosa, V., *et al*. (2022). Tip-Enhanced Raman Spectroscopy of Semiconductor InP-InGaP hetero-structured Nanowires. *Quantum Matter International Conference - QUANTUMatter 2022 (Barcelona, Spain)*

[2] Mediavilla, I., Hinojosa, V., *et al*. (2022). Unveiling the light emission of InP-InGaP heterostructured nanowires. *Quantum Matter International Conference - QUANTUMatter 2022 (Barcelona, Spain)*

[3] Serrano, J., Hinojosa, V., *et al*. (2022). Towards high performance solar cells: Unveiling the Light Emission of Semiconductor Nanowires (NWs). Seminar. Department of Applied Physics. *Universidad Autónoma de Madrid*, (Madrid, Spain) & *Institut Louis Néel*, (Grenoble, France).

Chapter 1

Introduction

An alarming fact is that the temperature of the Earth since 1981 has increased by 0.18 ºC per decade. This is twice larger than the data registered before 1980 which was 0.08 ºC per decade. According to the National Oceanic and Atmospheric Administration (NOAA) temperature, 2021 was the sixth warmest year on record.[1] Such unprecedented temperature records in human history have been undoubtfully ascribed to human activity and correlated to anthropogenic greenhouse emissions by the Intergovernmental Panel on Clima Change (IPCC). According to the IPCC 2022 report, we are set to pass the 1.5 ºC threshold by 2040 and only severe cuts in carbon emission can aid to prevent daring environmental consequences.[2] Energy has been reported to be the dominant contributor to climate change responsible for 60 % of total global greenhouse gas emissions.[3] International organizations invest and promote actions to stop the incessant global warming before reaching the point of no return, beyond which nothing could be done. The 193 countries that conform the United Nations (UN), approved the 2030 Agenda for Sustainable Development in September 2015. This agenda established a transformative vision towards economical, social, and environmental sustainability, a new road map, and a reference guide for the next years in which 17 goals were

agreed upon, the so-called Sustainable Development Goals (SDGs). The SDG # 7 calls to *"Ensure access to affordable, reliable, sustainable and modern energy for all"*.[3]

The transition from fossil fuels to renewable energies presents several challenges. The percentage of renewable energies in use is still very low. Worldwide fossil fuels use is 80 %, while 20 % corresponds to all the other energies as shown in Fig. 1.1.[4] In order to achieve the SDG # 7 of UN 2030 agenda, it is, therefore, imperative to focus more resources and dedication on 3a rapid transition from fossil fuels to renewable energies. Solar cells are made principally of silicon and, the cost of solar cell production is around 0.48-0.56 USD per Watt-peak.[5] The record in the efficiency of silicon solar cells using industrially-sized silicon wafers is 25.6 %.[6] In the commercial market, a solar panel has an efficiency of 16-21 %. There is a clear challenge to increase the efficiency of photovoltaic technology. One limiting factor of this low efficiency is the fact that a single solar cell, which is made of just one p-n junction, can convert only a fraction of the sunlight into useful energy.[7]

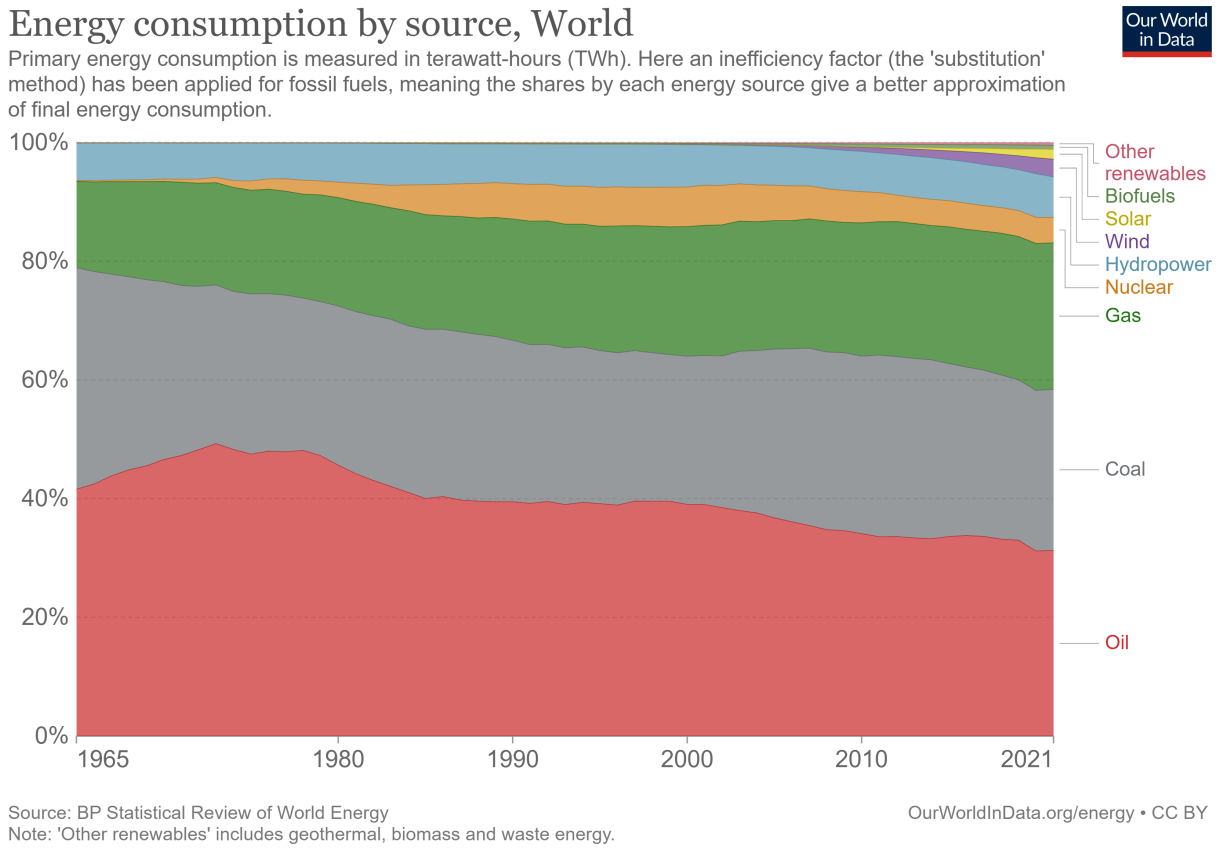

Figure 1.1: Worldwide energy consumption by sources. It displays our current dependence on high carbon emission sources. Taken from[4]

A way to improve the efficiency is taking advantage of a wider sun light spectrum absorption, in order to reduce the sunlight wasting, e.g., by using a combination of several cells.[8] This can be achieved with the so-called tandem solar cells. Figure 1.2 shows a monolithic GaInP/GaInAs/Ge triple-junction solar cell from Ref. 9. Tandem solar cells are one approach to exceeding the Shockley Queisser efficiency limits for single junction cells.[9,10] These kinds of solar cells reduce the two main losses in the energy transformation: (i) The thermalization of the excess energy provided by high-energy photons and (ii) transparency to the low energy photons.[10] The structure of tandem solar cells consists of stacks of p-n junctions, each of which is formed by a semiconductor

of different bandgap energy.[9,11] In that manner, each material absorbs within a spectral window of the sunlight, thus enhancing the overall absorption, and thereafter the efficiency.[9] The stack of the materials is made from top to bottom in order of decreasing bandgap. In that manner, the light with higher energy is absorbed by the top cells, while the lower energy light can reach the bottom cells.[9,11]

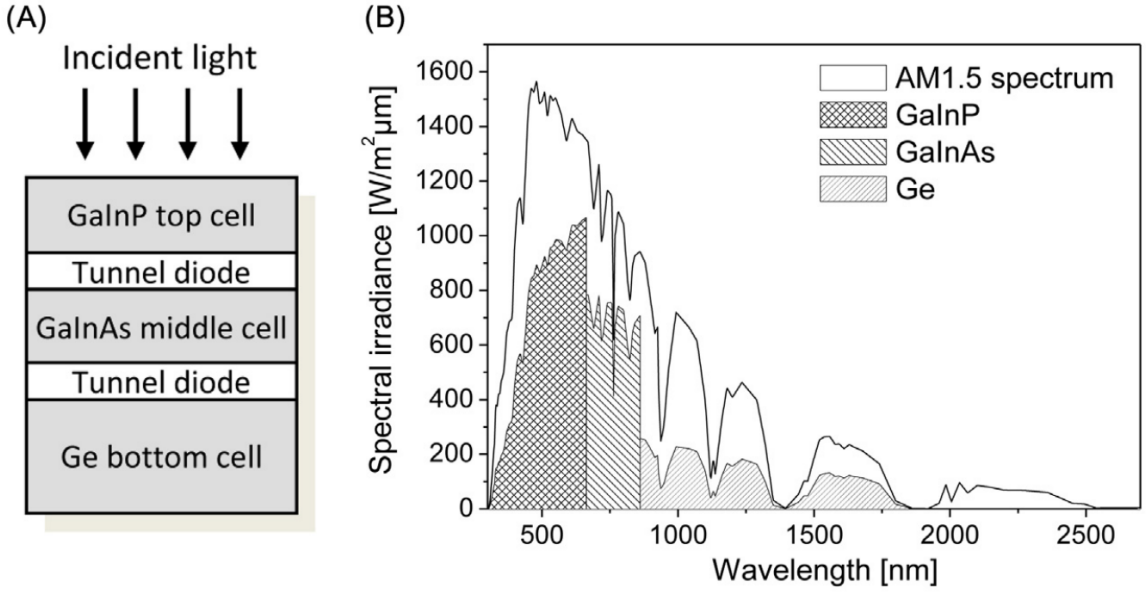

Figure 1.2: (A) Schematic structure of a monolithic GaInP/GaInAs/Ge triple-junction solar cell, and B) Spectral irradiance of the spectrum together with the parts of the spectrum that can be used by a triple-junction solar cell. Taken from Ref.4

Building solar cells with stacked crystalline materials for high-efficiency devices (free of defects) presents several challenges. In planar technology, the junctions of the cell must be done with lattice matched materials and similar thermal expansion coefficients.[9] These limitations constraint the number of candidates for achieving functional tandem solar cells, as the lattice matching conditions permit only a few combinations of materials.[12,13] The lattice mismatch between materials is a source

of extended defects that are detrimental to the device performance and reliability.[13] Moreover, the cost of tandem solar cells is substantially higher than the price of traditional silicon solar cells due to the more expensive fabrication process, and the scarce elements used in these cells, e.g. Ga and In.[14] These challenges concerning the fabrication of tandem solar cells demand the need for new approaches. Most of the challenges above mentioned can be circumvented by using semiconductor nanowires (NWs) instead of planar material.

Semiconductor NWs are promising materials for the next generation of solar cells.[15] There is a potential advantage of NWs over planar wafer-based or thin film solar cells in the photo-conversion process because of their geometry.[15] The advantages include strain relaxation because of the low dimension allowing the combination of materials that were incompatible in planar technologies, extreme light harvesting, increased defect tolerance, improved band gap tuning, and reduced reflection.[15,16] Nanowires present an exceptional tolerance to epitaxial stress with the underlying grown substrate. Thus, they can be grown in substrates not necessarily crystalline, which are very costly.[17] All these advantages allow us to reduce the cost per-Watt-peak in the building of solar cells.[15] Using III-V NWs, the saving of expensive materials is enormous as one can reach the same light absorption with only 5% of raw materials consumption concerning the planar technology.[18]

Beyond the application of NWs in energy generation, they also have plenty of applications in other fields. In the field of electronics, Field Effect Transistors (FETs) have been fabricated with NWs.[19] The use of NWs in electronics comes from the controllable dimensions of NWs, which enables adding functionalities. The aspect ratio and the nanoscale provide new optical, electrical, mechanical, and thermal properties, which allow tailoring the active regions to the requirements of the specific device.[20] Besides, NWs also maintain the bulk property of doping in a controlled way, essential for their use in devices, and providing a critical degree of freedom

needed for practical device applications. Silicon NW were the first NWs used to made FETs. They demonstrated the ability to control carrier type and density through a back-gated geometry, although the mobility and the transconductance were low. Silicon NWs has been used in conventional silicon technologies and for source drain contacts. In the same research line, it is relevant to understand the dopant distribution and effectiveness. The first contributions to controlling the carrier type and concentration of Si NWs drove to the creation of several devices, for this a deep understanding of the dopant activation and distribution in Si NWs has been achieved.[21] To mention one example, it has been reported that the surface states create charge depletion which limits the effective channel diameter. Therefore, a distinction between the morphological radius and the electronic radius is needed, and the last one is more accurate to define the charge-carrying cross-sectional area.

NWs also have been studied to use their properties to gain information about mobilities and carrier concentration along the NWs which act as active channels. This information could be used as a powerful quantitative comparative method between synthesis and growth techniques of similar materials. Defects such as vacancies can change abruptly the electronic behavior in NWs. In the case of ZnO NWs, oxygen vacancies changed the material from semiconductor to insulating.[22]

The surface of NWs contribute to interesting properties for sensor devices. While the first Si NWs research focused into maintain the pristine nature of the single crystal NW channel, now scientists have realized that the sensitivity of the surface is advantageous for sensing applications. In this context, chemical, biological, and molecular reactions might be detected at very low concentrations of active materials using NWs measuring the change in the electrical signal. Sensors based on SnO_2 NWs have shown very high efficiency detecting O_2 and CO_2 gases. On the surface of NWs, oxygen vacancies are produced as a result of the interaction with combustible gases. These vacancies act like donors and increase the conductivity of the NW. Similar works have

also demonstrated high sensitivity and fast answers to changes in air humidity using SnO_2. ZnO NWs have been used to detect ethanol, oxygen, and hydrogen. In the biological field, Si NWs are candidates to be functionalized to generate very specific sensors for biological receptor groups in addition to molecular detection. For example, Si NWs functionalized with peptide nuclei acids (PNAs) receptors have shown a very sensitive detection to DNA in real-time.[22]

Nanowires have a great impact in the field of photonics. They are natural one-dimensional optical waveguides, and they have a subwavelength diameter. In the case of chemically synthesized NWs, photons propagate along the wires with low losses because of their atomically smooth side walls. This has a great impact on photonic circuits because the light generated from miniaturized sources needs to be captured and driven to the next circuit parts. NWs can exhibit active functions as compared to simply passive waveguides, and they also have shown strong light-matter interaction through laterally confined resonances. The NWs with subwavelength diameters could be considered as a scaled-down version of dielectric microcylinder resonators. It means that they can trap light and behave as optical nanoantennas. However, the confined resonant modes of NWs tend to be leaky and interact effectively with the outside media.[22]

Each of these applications takes advantage of different characteristics of the NWs. Some of them require doping, a different configuration of the heterojunctions, different bandgaps, a thorough understanding of the role of defects, specific functionalization, etc. Many of these aspects can be analyzed with spatially-resolved optical characterization techniques, such as micro-Raman, micro-photoluminescence, in which the spatial resolution in confocal configuration is below the micrometer boosting the spatial resolution down to the nanometric scale can be achieved with the techniques of tip-enhanced Raman spectroscopy (TERS) and tip-enhanced photoluminescence (TEPL).

Raman spectroscopy is standardly used for the characterization of semiconductor materials. The Raman effect in solids consists of an inelastic light scattering involving phonons. Raman spectroscopy provides information about physical factors that can disturb the local order or modify the interatomic distances because lattice vibrations are very sensitive to the local structure and lattice environment. Therefore, Raman spectroscopy is a powerful technique that supplies relevant information about crystal orientation, lattice temperature, symmetry breakdown, strain, chemical composition, as well as electronic, and thermal properties. There is no doubt that this information is vital to build up a diagnosis about the properties of the semiconductors, or to identify the changes induced during the fabrication device processes.

Raman scattering is a second order optical phenomenon, in contrast to photoluminescence (PL) which is a first order optical phenomenon, thus giving much more intense signals than Raman.[23] The main expected information of a semiconductor material obtained from PL is the spontaneous interband emission, and the emission arising from in-gap states associated with defects and impurities. The luminescence emission arises from the recombination of the excess carriers generated by the excitation, in the case of PL the excitation is done with light of energy above the bandgap. The luminescence signal is related to the ratio between radiative and non-radiative recombinations, e.g. surface recombination, which is crucial in NWs.

Raman and PL provide useful information about semiconductor materials at the slightly sub-micrometric scale using a confocal microscope. When a higher spatial resolution is required, TERS and TEPL techniques can be used to scale down the resolution to a few nanometers. These techniques combine the optical spectroscopies of Raman and PL with an Atomic Force Microscope (AFM). In that manner, the incident laser beam is focused on a silicon AFM tip coated with gold or silver. The tip-enhances the electromagnetic field and localizes it at a dimension close to the tip

diameter, thus allowing the nanometer resolution.

Regarding all the reasons exposed above, this work aims at obtaining relevant information on hetero-structured NWs of indium phosphide (InP)/indium gallium phosphide (InGaP) forming structures for tandem solar cells with special emphasis paid to the tunnel junction, which require narrow depletion regions achieved by degenerate doping of the p and n sides. Obtaining information about tunnel junction is challenging because of its small dimension, only a few nanometers thick, and the fact that heavy doping can produce changes in the morphology and the crystallographic phase of the NW.

In Chapter 2 we will describe the structure of the InP/InGaP NWs as well as the characterization techniques used with their measurement parameters. Chapter 3 is devoted to the presentation and discussion of the results. Finally, in Chapter 4 we will summarize all the relevant information reported here and give a few suggestions for further research.

Chapter 2

Methodology

2.1 Sample description and preparation

In this work, nanowires (NWs) were provided by Prof. Magnus Borgström from NanoLund: Center for Nanoscience of the University of Lund (Sweden). Nanowires were grown on a silicon substrate using the Vapor-Liquid Solid (VLS) method with gold droplets as catalysts. This growth technique is one of the most common and precise ones for fabricating NWs because it allows high accuracy in the NW diameter and composition. It consists of heating the Au droplet above the eutectic temperature ($\approx$ 363 ºC) in an inert atmosphere. The growth process starts with the supply of the precursors. The Au droplet catalyzes the precursor decomposition. As the precursor keeps flowing, the concentrations of the constituent elements increase in the liquid catalysts particle until supersaturation. Then, the crystallization of the semiconductors takes place, and the NW starts growing at the interface of the gold droplet with the semiconductor. The ratio of the precursor fluxes determines the concentration, while the Au droplet size determines the NW diameter.

The NWs are axially hetero-structured and formed by a bottom cell made of n-i-p InP, a p^+

InGaP-n^+ InP tunnel junction, and an InGaP n-i-p top cell. The graphical scheme of the NW is shown in figure 2.1.

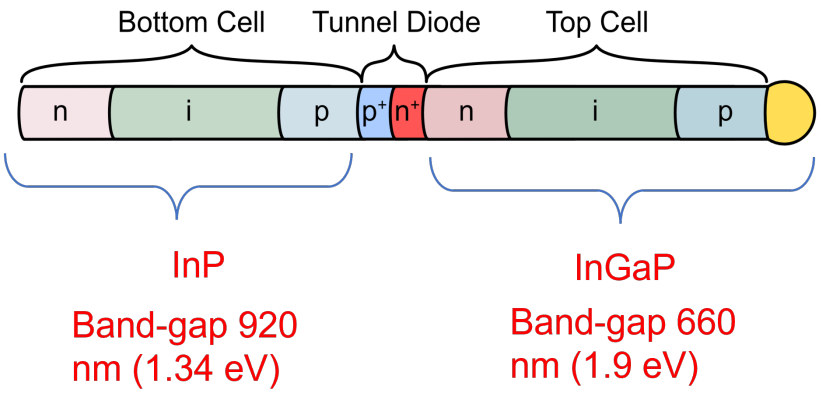

Figure 2.1: Structure of the investigated NWs. The bottom part corresponds to indium phosphide (InP), the top corresponds to indium gallium phosphide (InGaP), and between the two structures there is a tunnel junction

The as grown sample contained a set of multiple NWs on a substrate as shown in the Scanning Electron Microscope image, Figure 2.2. The contrast in the Scanning Electron Microscopy (SEM) image shows the three main parts of the NW with different contrast: the InP bottom cell, the bright contrasted tunnel junction because of the high carrier density, and the top cell. At the end of the NW there is a spherical cap corresponding to the gold droplet. The study will be carried out on single NW, therefore, one needs to separate them from the substrate. Their manipulation was done by contacting the sample with a piece of optical paper and then contacting the optic paper on a silicon substrate coated with gold. The metallic substrate has two advantages, on one side it enhances the Raman signal arising from the NW, and on the other side, it behaves as a heat sink allowing to dissipate the heat induced by the laser beam during the optical spectroscopy measurements on the NWs. The NWs lay down on this substrate and are ready for single NW analysis in the microscope stage.

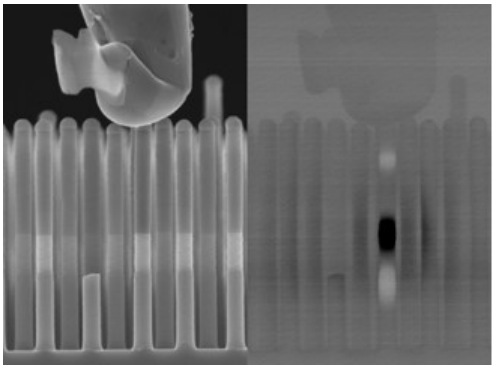

Figure 2.2: SEM image of InP/InGaP NWs provided by NanoLund group

2.2 Experimental techniques

2.3 Micro-Raman spectroscopy

Raman spectroscopy is widely used as an optical characterization tool for investigating semiconductors in bulk, thin film, nanostructured, and device forms. When light interacts with a solid, several phenomena take place, e.g. reflection, absorption, and light scattering. The light scattering can be either elastic (Rayleigh), or inelastic. The Raman effect is an inelastic scattering phenomenon in which elementary excitation energy quantas of the solid are exchanged with the excitation electromagnetic wave. In Raman spectroscopy, those elementary excitations are optical phonons. The Raman effect consists of the coupling of the electromagnetic field of the incident light with the optical phonons through the induced electric dipole moment. The incident photons, characterized by their energy, wavevector, and polarization, are inelastically scattered by the crystal. The inelastic component (Raman) of the outgoing light is characterized by its corresponding intensity, energy, wavevector, and polarization, which are determined by the structure and nature of the solid. The relation between the incident and the scattered light is governed by the corresponding

Raman scattering selection rules, which are determined by the lattice symmetry and the nature of the crystal.[24] The energy exchange between the incident light and the solid can only take the values of the phonon energies. When the lattice absorbs the energy necessary to excite a phonon the Stokes (S) component of the spectrum is observed, whereas the release of a phonon to the electromagnetic wave results in the anti-Stokes (AS) component of the Raman spectrum. Usually, Raman experiments deal with the S component, because its intensity at room temperature is several times that of the AS component.

Raman spectra were acquired using a HORIBA Labram Raman Soleil apparatus. First, an optical image was recorded in order to localize the NWs and its orientation. We then selected some NWs and we performed measurements to optimize the signal. The first feature we noticed is that the NWs oriented parallel to the laser polarization gives the best Raman signal. The range of measurement was selected between 250 and 450 cm^{-1} which is the range where the characteristic Raman peaks appear (more detail in the next section). Line-scans along the NW with a 532 nm laser at 0.57 mW were carried out, using a 100 X objective. The scan along the NW axis was taken at a constant step of 0.2 μm. The acquisition time was 1 s. The detail of all measurement parameters is shown in table 2.1

2.4 Micro-photoluminescence (PL)

The basic principle of photoluminescence (PL) is the radiative recombination of excess electron-hole pairs. The excitation is carried out with light of energy above the bandgap, this excitation generates electron-hole pairs, which the radiative recombination constitutes the luminescence emission. Different recombination mechanisms exist. The recombination of an electron of the conduction band with a hole of the valence band gives an emission with the bandgap energy.

Other transitions can occur in the presence of in-gap states due to impurities and defects. The PL intensity is governed by the ratio between the radiative and non-radiative recombination rates. The non-radiative recombination is associated with defects and surface recombination, the last one is very important for NWs because of its aspect ratio with large surface to volume ratio. A high luminescence emission means a material with a low concentration of defects, while a low luminescence emission is associated with a defect-rich material.[23,25]

Photoluminescence measurements were made with the same HORIBA Labram Soleil apparatus as the Raman experiments. The sample was excited with a 532 nm wavelength laser using a power of 532 nm at 5.7 μW. In this case, we used a grating of 150 lines/mm, a 100 X objective. A similar scan along the NW axis was performed for the PL measurements. All the measurement parameters are displayed in Table 2.1.

2.5 Tip-enhanced Raman spectroscopy (TERS)

The physical process in tip-enhanced Raman spectroscopy (TERS) is the same as the one we described in section 2.3. The advantage is that TERS brings Raman spectroscopy into nanoscale spatial resolution. In this technique, the Raman spectrometer is coupled to an Atomic Force Microscope (AFM) modulus. The TERS system uses a metallic tip, commonly made of silver or gold. The tip is illuminated by a laser beam. The interaction between the laser beam and the tip generates a strong localized near field around the tip apex. The local field enhancement permits measuring the Raman spectrum of very small volumes of matter, allowing a resolution of a few nanometers. The resolution is determined by the tip size and its interaction with the laser beam. The tip acts as a nano-source of light behaving as a local field enhancer (by a factor of 10^3 -10^7).[26]

TERS measurements were performed on the HORIBA Labram Soleil apparatus. In this case,

an AFM module optically coupled to the spectrometer was used. For TERS measurements we used a gold coated Si AFM tip with a working frequency of 150 Hz, and a red wavelength excitation laser (638 nm), instead of the 532 nm laser, because the later laser could damage the gold coating. We performed a map scan of the NW and some specific point measurements in a contact mode. Similar acquisition parameters as used for μ-Raman measurements were employed for collecting the TERS signal. The difference with micro-Raman measurements concerns the step size that was downscaled to 40 nm instead of 200 nm. Besides, the electromagnetic field around the tip has different characteristics in terms of polarization and incident geometry than the laser beam used in micro-Raman thus yielding different scattering selection rules. This must be considered when comparing μ- Raman and TERS spectra, as we will mention in Chapter 3. A summarized parameter description is detailed in Table 2.1 with all the setup information.

2.6 Tip-enhanced photoluminescence (TEPL)

Tip-enhanced photoluminescence (TEPL) combines the earlier characterization techniques described. This also uses the optomechanical coupling with the AFM modulus and the working principle is the same as the one described in section 2.4. Tip-enhanced photoluminescence measurements were made in a similar experimental arrangement as that described for the TERS measurements, section 2.5. The diffraction grating had 150 lines/mm, and the acquisition time was 0.1 s to avoid detector saturation. The details of the main measurement parameters are shown in Table 2.1.

Table 2.1: Measurement parameters of Micro Raman, Micro photoluminiscence, TERS, and TEPL.

Parameter	Value			
	Micro-Raman	**Micro-PL**	**TERS**	**TEPL**
Laser	532 nm	532 nm	638 nm	638 nm
Power	0.57 mW	0.57 μW	20 μW	20 μW
Objective	100 X	100 X	100 X	100 X
Hole	200 μ m	200 μ m	200 μ m	200 μ m
Grating	2400 l/mm	150 l/mm	2400 l/mm	150 l/mm
Detector	CCD	CCD	CCD	CCD
Spatial resolution	< 1 μm	> 1 μm	$\approx$ 10-20 nm	$\geq$ 20 nm
Acquisition time	1 s	1 s	1 s	0.1 s

2.7 Energy-dispersive X-ray analysis

The energy-dispersive X-ray (EDX) spectroscopy is a fundamental technique for elemental analysis and chemical composition determination, associated with electron microscopy. It uses X-rays generated by an electron beam to irradiate the sample.[27] Then, according to the characteristics and nature of the elements present in the sample, it reveals their identity.[28]

In order to understand better the chemical composition and distribution of In, and Ga along the NW, we performed an EDX analysis. This experiment took place at the Scientific Park of the University of Valladolid. The service was made by the microscopy unit with a FEI-QUANTA

200FEG SEM equipped with a field emission gun with Schottky filament. The image was obtained using an acceleration voltage of 20 kV and the ADC1 detector.

Chapter 3

Results & Discussion

3.1 Micro-Raman experiments

The Raman spectrum of InGaP is reported to have a modified, two-mode behavior.[29] The characteristic Raman spectrum of GaAs lattice matched $In_xGA_{1-x}P$ ($x \approx 0.5$) consists of three main peaks. The first peak approximately at 330 cm^{-1} corresponds to a transverse optical phonon (InGaP-TO) labeled as TO_1. The second peak usually appearing around 360 cm^{-1} is typically assigned to an InP-like longitudinal optical phonon (InP-like LO) henceforth labeled as LO_2. The third one peaks around 380 cm^{-1}, which corresponds to a GaP-like longitudinal optical mode (GaP-like LO) henceforth labeled LO_1.[30] An additional mode has been observed at approximately 364 cm^{-1}, which corresponds to a second transverse optic mode (TO_2), it is scarcely observed due to its weak mode strength, at least one order of magnitude lower than the mode strength of the TO_1 mode.[30] A reference spectrum of $In_{0.35}Ga_{0.65}P$ with the described modes is displayed in Fig. 3.1 The LO_1 Raman shift is not affected by the spontaneous order.[31] Therefore, in a strain free situation, the LO_1 mode frequency can be used to study the composition of the alloy. The frequency position

of the LO_1 mode in the $In_xGa_{1-x}P$ alloy shifts with x. The shift corresponds approximately to 0.7 cm^{-1} per Ga percentage around the GaAs lattice-matched composition range. This behavior in an extended composition range follows a non-linear dependence with the composition.[32] The relationships describing the phonon frequencies with composition are the following:

$$\omega_{LO_1} = 404.99 - 37.97x - 18.18x^2(cm^{-1})$$

$$\omega_{LO_2} = 394.59 - 80.36x + 30.26x^2(cm^{-1})$$

$$\omega_{TO_1} = 368.82 - 88.95x - 6.72x^2(cm^{-1})$$

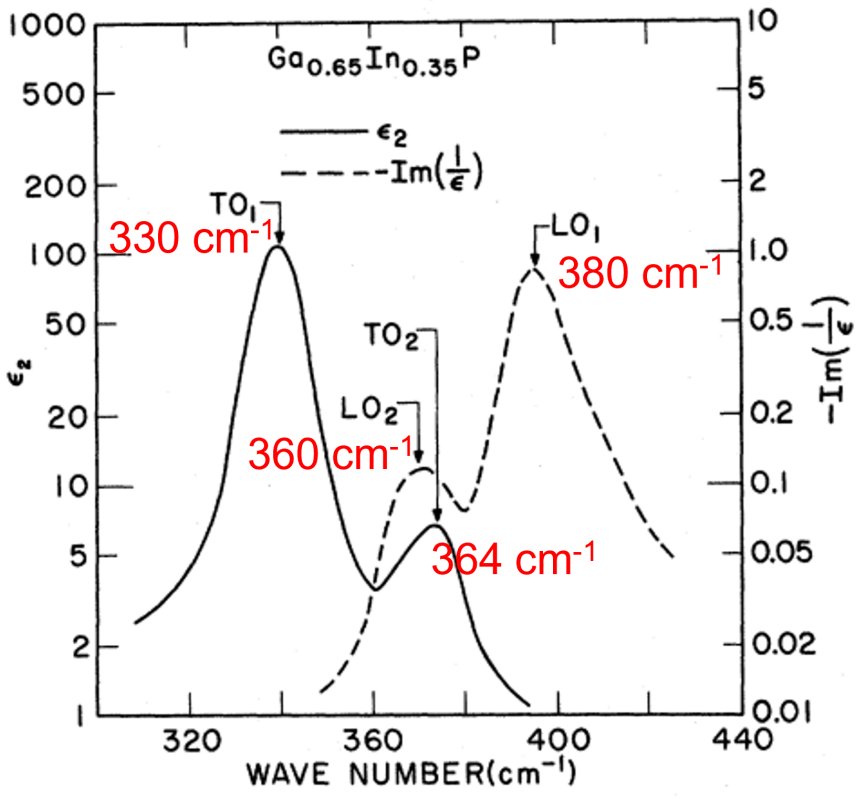

Figure 3.1: Reference Raman spectrum of $In_{0.35}Ga_{0.65}P$ adapted from Ref.[30]

The nanowires (NWs) studied herein have a nominal composition of 35% In. A direct bandgap is predicted for such values of In concentration though they are very close to the critical value for

direct-indirect bandgap transition of InGaP alloy.

The Raman spectrum of InGaP in the NWs presents the characteristic Raman modes described above. Because the NWs lie down on the substrate, the Raman selection rules for zinc blende structure only permit to observe the TO modes, being the LO modes forbidden in such scattering configuration.[33] The NWs were scanned by the laser beam along its axis in steps of 200 nm.The spectra obtained along the scan of a 10 μm long NW are plotted in Fig. 3.3. The optical image of the NW with red arrows indicating the scan direction is also shown. The NW diameter is below the diffraction limit, therefore, it would not be observed under the optical resolution of the optical microscope; however, the NW behaves as a nanolens rendering it visible to the optical microscope.[34] The Raman spectra reveal interesting features about the NWs.

Three individual spectra are analyzed separately in order to identify the main Raman mode contributions in different sections of the NW. One spectrum of the InP bottom cell, one for the tunnel junction region, and one for the InGaP top cell. They were treated with PeakFit software and they are plotted with their corresponding fits in Figure 3.1. The spectral parameters are summarized in Table 3.1

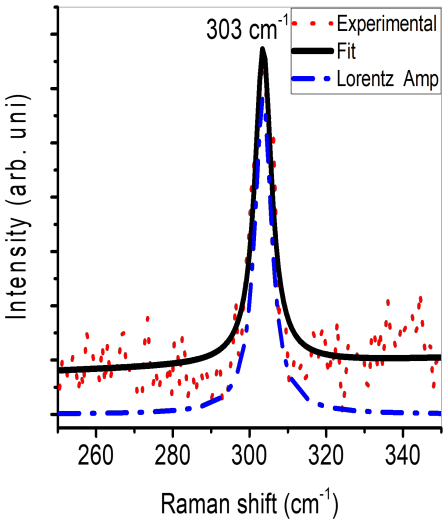

(a) InP (TO)

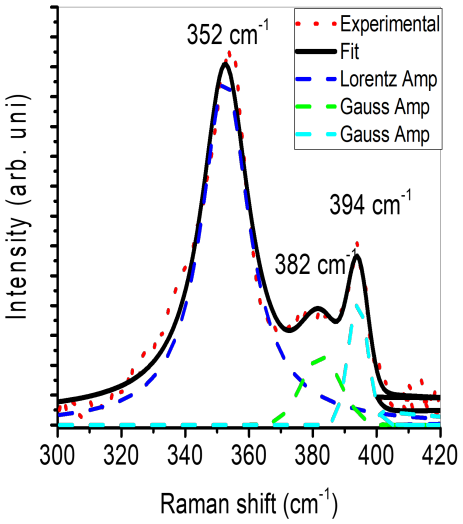

(b) p^+-type plasmon

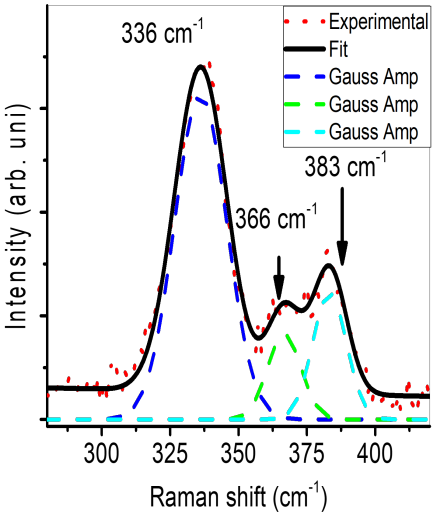

(c) InGaP (TO_1, LO_2, and LO_1)

Figure 3.2: Experimental Raman spectra with their corresponding fits a) InP TO mode of the InP bottom cell b) Tunnel diode c) InGaP top cell

Table 3.1: Peak position and Full Width-Half Maximum (FWHM) of each vibrational mode of InP/InGaP NWs according to the fit

	Position	Intensity	FWHM	Assigment
InP region	303.5	116	5.3	TO (InP)
	352.5	1153	18.1	p^+-type plasmon
Tunnel diode	382.6	228	14.5	LO_2
	394.2	406	7.43	LO_1
	336	469	22.5	TO_1
InGaP region	366	122	14.6	TO_2
	383	182	14.64	LO_1

The InP bottom cell shows a phonon mode at $\approx$ 303 cm^{-1}, corresponding to the transverse optic phonon (TO) of the InP. The longitudinal optical mode (LO) ($\approx$ 346 $cm^{-}1$) was not observed because the NW is lying horizontally on the substrate, corresponding to an exposition of the (110) lateral faces of the NW to the laser beam. This means that the NW has a zinc blende structure, and the Raman selection rules are satistied. Furthermore, one does not observe Raman modes related to the wurtzite phase, frequently present in III-V NWs, this supports again the zinc blende structure of the NW. The wurtzite phase seems to be fully absent, or if any it will be very local. When the laser enters the tunnel diode one observes two fascinating facts. First, the intensity of the TO_1 mode is strongly reduced. Simultaneously, LO_1 and LO_2 modes are observed. Additionally, a very intense peak around 354 cm^{-1} is observed. Note that the composition of InGaP can be controlled by the

LO_1 peak frequency, it can present some fluctuations, mainly associated with doping. One observes that for the p-type (Zn doped) zones the LO_1 mode appears around 393 cm^{-1}, which corresponds to In composition of $\approx$ 25%, well below the nominal concentration given by the growers (35%). For the n-type region (S doped) the In composition is close to the nominal 35%. If one analyzes this peak one can argue that it corresponds to an LO-phonon plasmon coupled (LOPC) mode. For a detailed analysis of the LOPC modes in the Raman spectrum of polar semiconductors the reader is addressed to Pages, O. *et al*, 1996.[35] The spectral position of this peak, between the LO and TO modes, reveals that it is due to a damped hole plasmon, therefore, it arises from the p+ side of the tunnel junction. The LOPC modes follow the same selection rule as the LO phonons. The observation of the LOPC and LO phonon modes, and the non observation of the TO modes at the p-InP/p+-InGaP heterojunction evidence the breakdown of the Raman selection rules. The second effect is the strong resonance observed at the p-InP/p^+InGaP hetero-structure, which results in the significant local enhancement of the LOPC intensity. Note that the LO phonon modes also appear but with low intensity, because they are screened by the plasmons. The dielectric mismatch at the heterojunction produces the resonance giving a strong local enhancement of the electromagnetic field.[34,36,37] Once the laser beam crosses the tunnel junction and enters the top InGaP cell the TO modes reappear in the Raman spectra, recovering the Raman selection rules for backscattering on the (110) surface. The inversion of the selection rule is also appreciated at the end of the NW, at the junction between InGaP and the gold droplet, where dielectric mismatch produces the electromagnetic field enhancement, although less intense than that observed in the tunnel junction. The very local enhancement of the electromagnetic field at the p-side of the tunnel junction produces a sharp gradient of the electric field, which is responsible for the selection rule breakdown.[38]

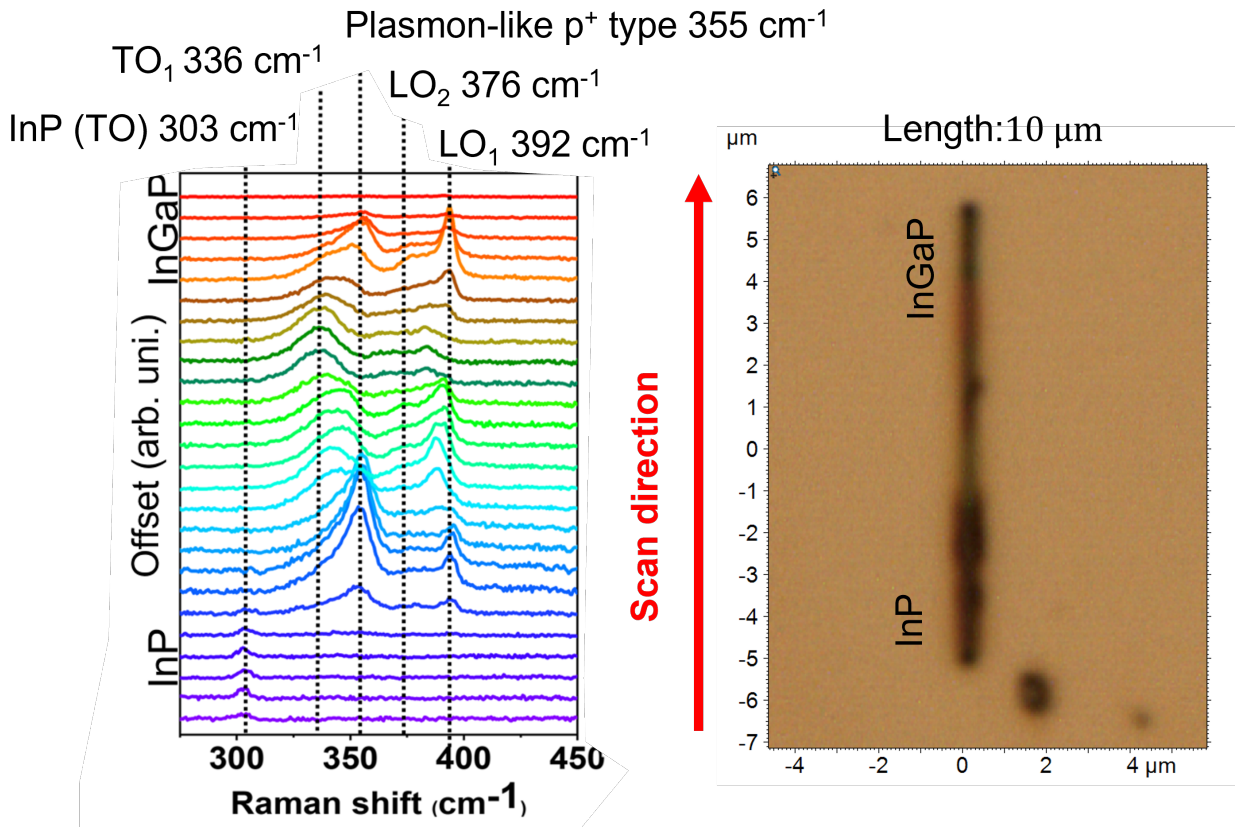

Figure 3.3: Optical image of the NW, and Raman spectra recorded along the InP/InGaP NW axis in steps of 200 nm. The red arrow shows the scan direction in both: the optical image and in the Raman waterfall spectra plot. The dot lines show where the modes appear with their corresponding assignment

3.2 Micro-photoluminescence experiments

Indium phosphide as well as InGaP present characteristic photoluminescence bands related to their respective band-gaps. InP has a band-gap of 1.34 eV at room temperature, thus the intrinsic emission band peak is around 925 nm.[39] The bandgap of InGaP depends on the alloy composition. For GaAs lattice matched InGaP ($In_{0.504}Ga_{0.494}$) the intrinsic emission is around 636 nm.[40] Figure 3.4 shows the photoluminescence (PL) spectra in a waterfall graph recorded along the NW axis.

The measurements were done at 300K. In the spectra, one can see the strong emission in the bottom cell, while the emission of the top cell based on InGaP appears very weak. For better observation, the spectra of the bottom cell were plotted separately from the spectra of the top cell, Fig. 3.5. The most intense band in the bottom cell peaks at 775 nm. The spectra that correspond to the InP cell show the mentioned band at 775 nm, which does not arise from InP, because of the higher emission energy concerning the InP bandgap. Furthermore, the band shift changes along the bottom cell. One can argue that this emission is due to a parasitic InGaP layer grown laterally, the low energy emission suggests that this layer is In rich. The tapered shape of the NW evidences the lateral parasitic deposition.

The composition of the parasitic InGaP shell around the bottom cell seems inhomogeneous along the NW. Regarding the top cell, one observes broad structured bands between 600 and 700 nm. The fluctuations observed along the NW obey some compositional changes and doping, the presence of low energy tails suggest also the presence of defects. The very weak emission can be related to the fact that the InGaP composition is close to the direct indirect bandgap cross point. From the Raman data, one can assert that the p-doped parts of the NW lye in indirect band gap composition, this suggests that the incorporation of Zn slows down the incorporation of In leading to Ga rich InGaP alloy, both in the tunnel junction, p side, and the end of the NW in the p-side of the top cell.

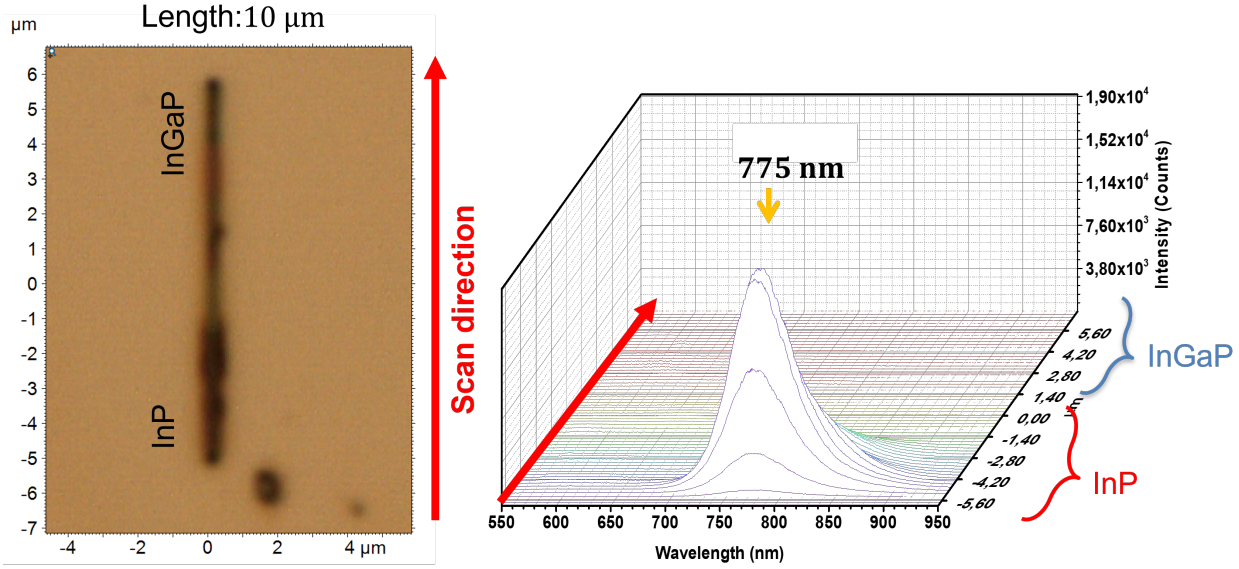

Figure 3.4: Photoluminescence line-scan spectra of InP/InGaP NW with its corresponding optical image. The red arrows represents the direction of the line scan. Brackets separate the spectra that corresponds to InP cell and InGaP cell.

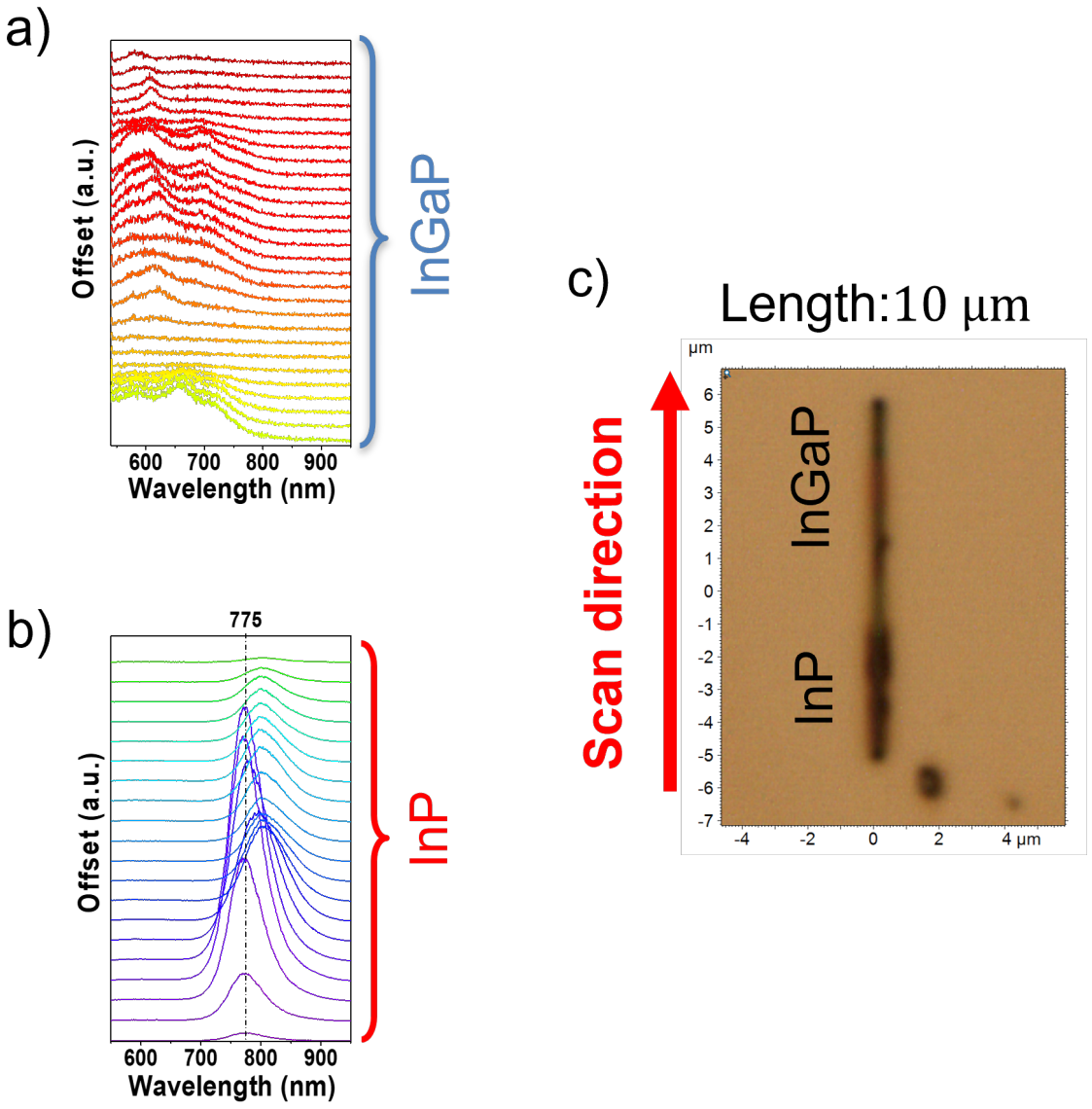

Figure 3.5: Detailed PL spectra of a) the InP bottom cell and b) the InGaP top cell. c) shows the scan direction along the NW with the red arrow

3.3 Tip-enhanced Raman experiments

In the field of nanostructures like NWs, the surface is very relevant to the properties of the NW. The near field of tip-enhanced Raman spectroscopy (TERS) allows for the analysis of a volume close to the surface. Furthermore, the use of a nanometer size gold coated tip focus field permits not only to

amplify the optical signal but also to scale the spatial resolution down to the nanometer size. Spatial resolutions down to 5 nm have been reported.[41] This can supply very useful information about the optical properties of hetero-structured NWs. Taking advantage of the nanometric spatial resolution of TERS we made six-point measurements along the NW. They are marked in the Atomic Force Microscope (AFM) image of the 10 μm long NW (Figure 3.6). The red crosses correspond to the points where the AFM tip was focused for acquiring the TERS spectra.

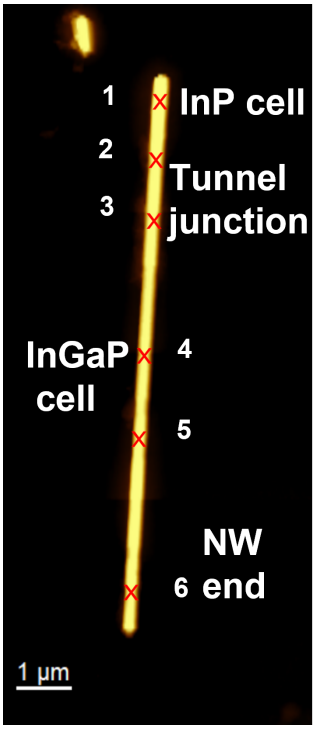

Figure 3.6: AFM image of a 10 μm length InP/InGaP NW with the points where the TERS measurements were performed

Figure 3.7 shows the corresponding spectra of the red marks in the figure 3.6. Panels #1 and #2 display the Raman spectra of the InP cell. In contrast with the micro-Raman, it shows the transversal and the longitudinal optical modes of InP labeled TO and LO, respectively. The InP-TO appears at 303 cm^{-1} and the InP-LO at 343 cm^{-1}. These spectra show two additional bands at 353 cm^{-1} and 391 cm^{-1} which correspond phonon modes related to the parasitic InGaP layer deposited

on the bottom cell walls. Note that these bands were not observed in the micro-Raman spectra of the bottom cell. This shows that the shell layer, which is very thin, a few nanometers, can be detected by the near field of TERS measurements, while, in the conventional micro-Raman spectrum, this thin layer has not enough scattering volume to give a Raman signal enough intense to be observed. These features agree well with the picture of the parasitic InGaP shell described earlier in the PL results. The spectrum #3 was taken at the tunnel junction and the p^+ type plasmon mode at 355 cm^{-1} is revealed together with the enhancement of the Raman signal. Spectra #4 and #5 correspond to the top InGaP cell, and they show the three expected Raman bands at 338 cm^{-1}, 367 cm^{-1}, and 385 cm^{-1} that correspond to the TO_1, LO_2, and LO_1 modes respectively. The last spectrum #6 corresponds to the end of the NW and it also displays a p^+ type plasmon mode at 355 cm^{-1}. This mode appears because of the dielectric mismatch between the p-doped InGaP section and the gold droplet.

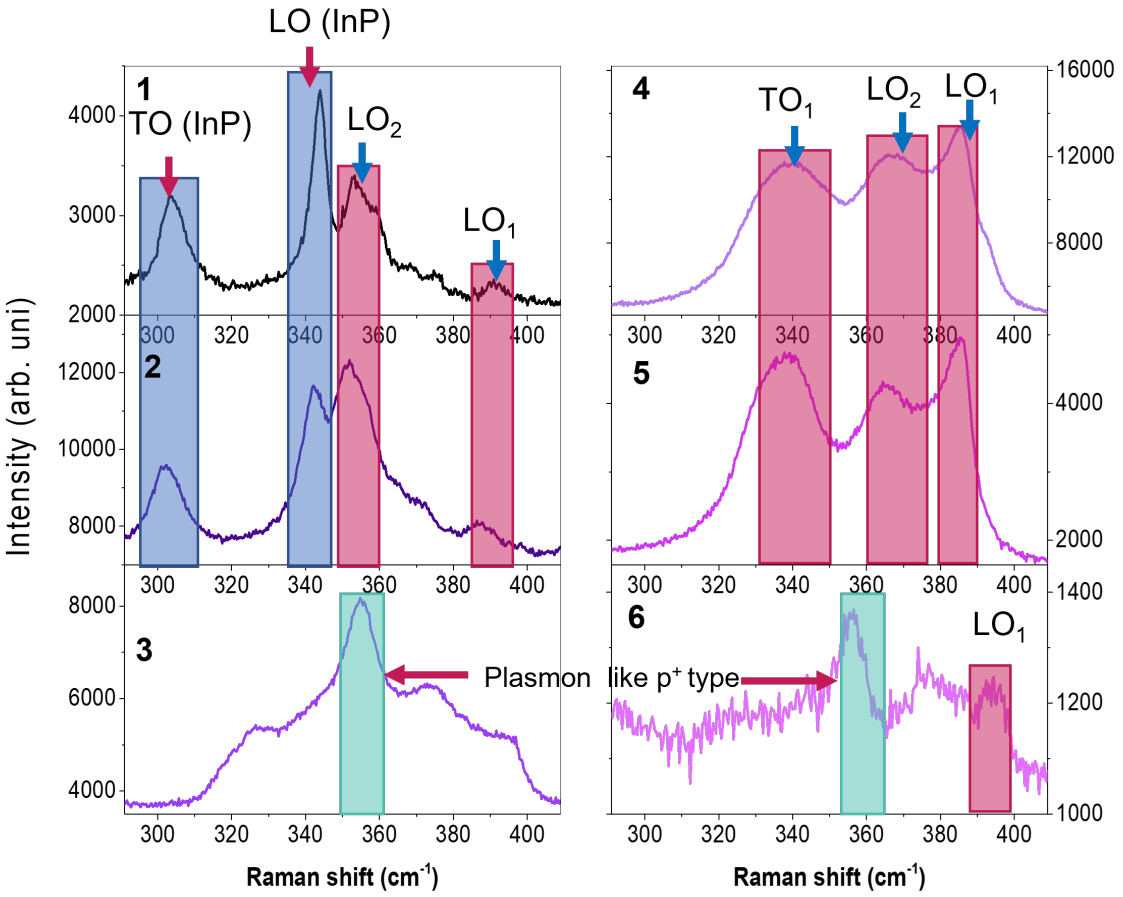

Figure 3.7: TERS spectra at the point marked by red crosses in the AFM image of Fig. 3.6. Spectra #1 and #2 were recorded on the InP bottom cell. Spectrum #3 corresponds to the tunnel diode. Spectra #4 to #6 correspond to the InGaP top cell. The spectra #6 corresponds to the end of the NW close to the gold droplet.

The spatial distribution of the Raman bands extracted from a TERS image is displayed in Figure 3.8. One can observe the tunnel junction through the LOPC mode image.

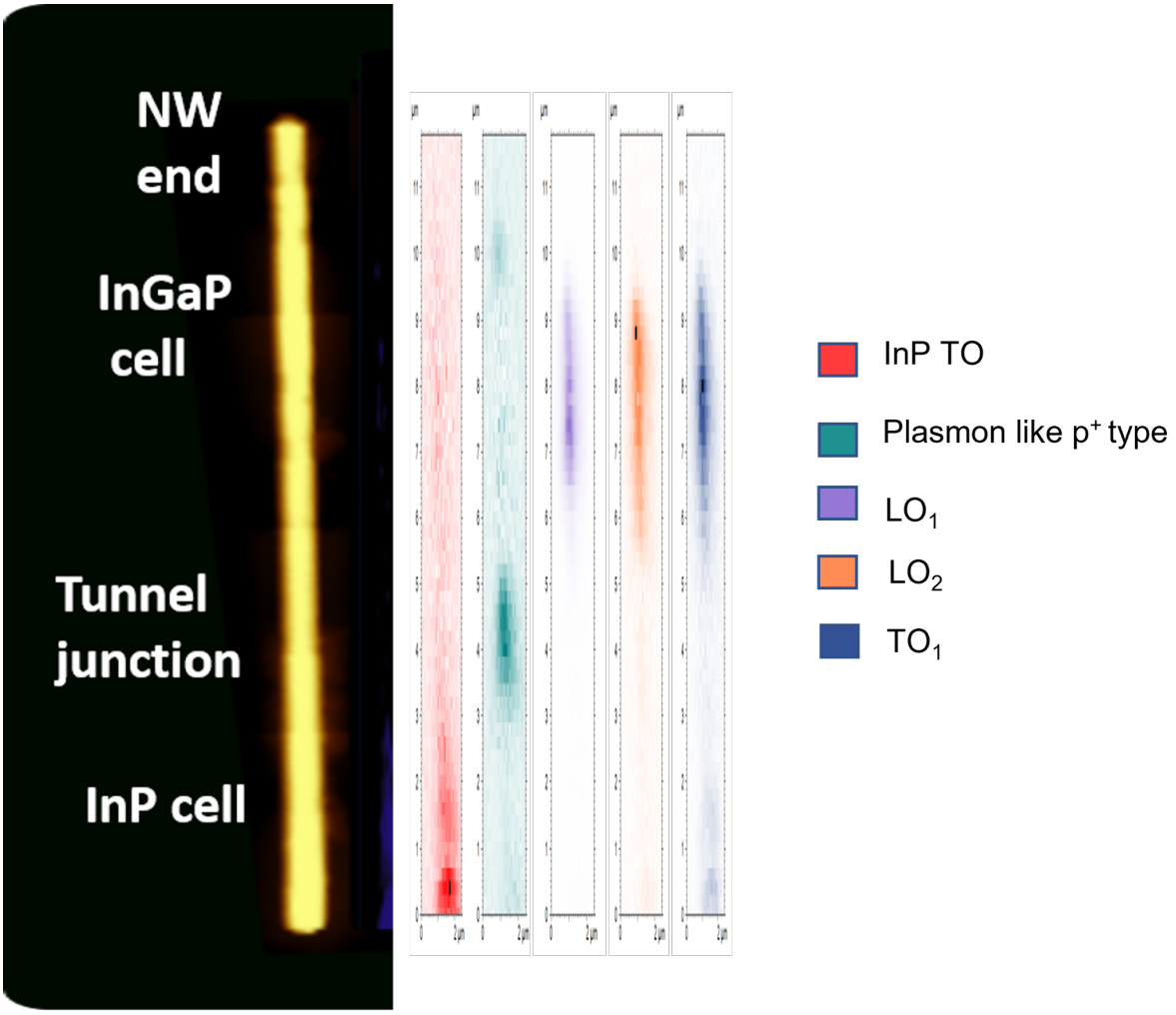

Figure 3.8: Tip-enhanced Raman map with the corresponding spatial distribution of the InP, tunnel diode, and InGaP representative bands along the NW axial direction

3.4 Tip-enhanced photoluminescence experiments

The tip-enhanced photoluminescence (TEPL) is achieved similarly as TERS, but in this case, the signal collected is the luminescence emission. A line scanning along the NW axis was carried out. The TEPL spectra are shown in Fig. 3.9. The lower spectra correspond to the InGaP top cell and the emission is almost zero, in good agreement with the micro-PL measurements, that gave

a very weak luminescence emission. Note that one risks having a lower signal in TEPL spectra concerning that obtained in micro-PL, because of the large weight of the surface recombination in the TERS measurement. When the laser impinges the tunnel diode region, on the contrary, we observe bands at 825 and <900 nm. Remembering that the tunnel junction did not emit because of its composition ($x \approx 0.25$) the two bands must be related to InGaP emissions, therefore, one can conclude that the parasitic InGaP shell is also grown around the tunnel junction. The TEPL signal increases at the heterojunction because of the resonance described previously. The 765 nm band observed in the bottom cell arises from the outer part of the InP bottom cell. TEPL is mostly probing the outer shells of the NW. In this sense micro PL and TEPL appear as complementary techniques. The bands between 600 and 700 nm previously found in micro PL in the top cell are not observed in TEPL, which is probably due to the higher weight of the surface recombination (non radiative) in TEPL than in micro PL.

The TEPL gives us information about the uppermost surface of the NW. These results support and reinforce the existence of the parasitic InGaP shell grown on the InP NW walls. The intense band detected at 765 nm in the bottom cell, and the almost zero signal of the InP core demonstrates that the parasitic shell is covering the lower part of the NW. Therefore, TEPL appears as a powerful tool for studying the outer shells of the NWs

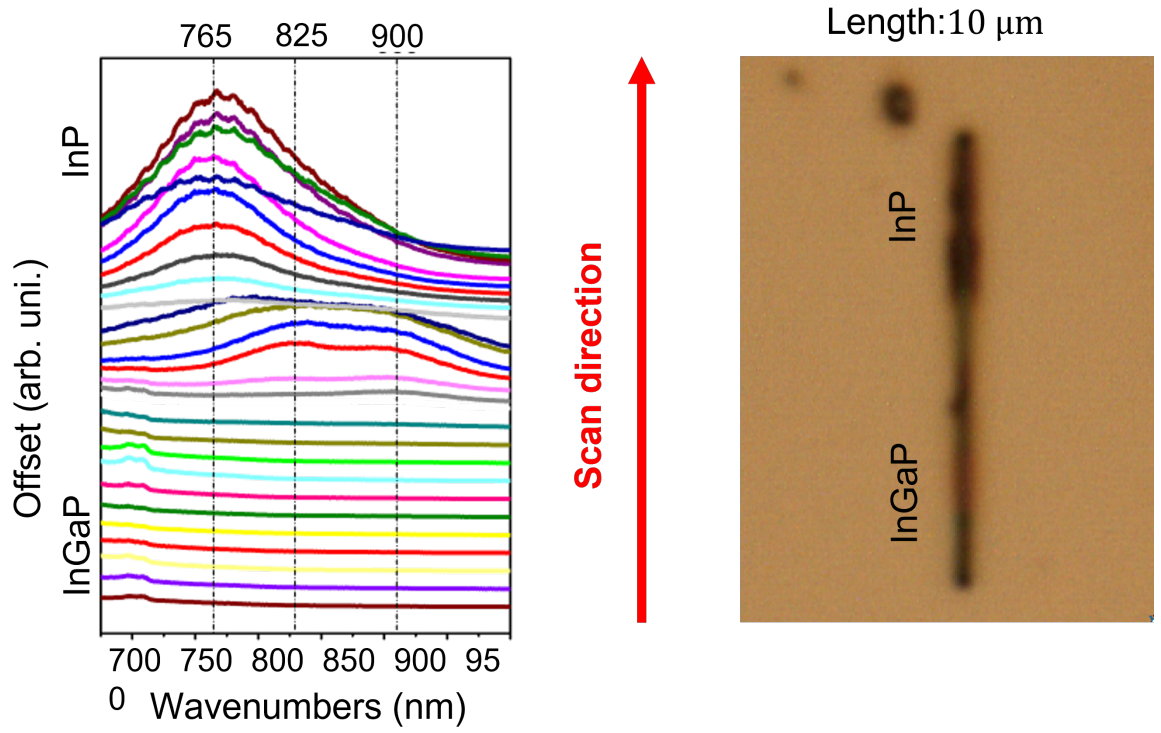

Figure 3.9: TEPL spectra of a 10 μm long InP/InGaP NW

3.5 Energy-dispersive X-ray analysis

The energy-dispersive X-ray (EDX) analysis was used for investigation of the NW chemical composition of the NW. The Scanning Electron Microscopy (SEM) image of the NW is shown in Fig. 3.10. The numbers indicate the points analyzed by EDX.

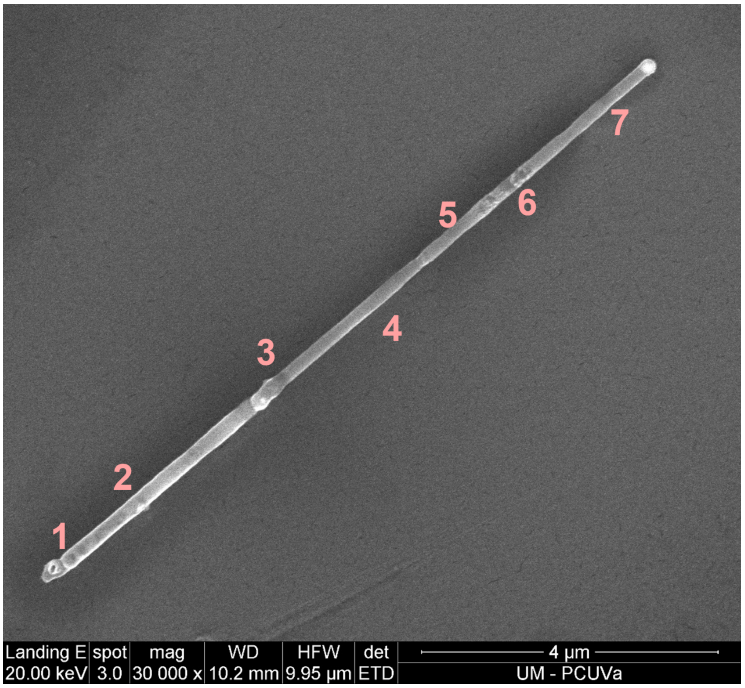

Figure 3.10: SEM image of the 10 μm length NW with 9 marks where we obtained the chemical composition using EDX analysis

Chemical analysis based on the EDX information allowed us to determine the In and Ga concentration along the NW. Table 3.2 displays the concentration of Ga and In on the 9 points marked in the Figure 3.10. The chemical concentration x of Ga atoms, and therefore that of In atoms, in the InGaP cell is quite homogeneous, with values close to $x \approx 0.37$. However, the concentration of Ga in the tunnel junction is $x \approx 0.27$. These composition data are in good agreement with those extracted from the frequency of the LO_1 mode in micro-Raman spectra.

Table 3.2: Chemical composition of In and Ga along the NW.

Point		1	2	3	4	5	6	7
Composition (0-1)	In	1	1	0.27	0.37	0.38	0.37	0.36
	Ga	0	0	0.72	0.63	0.62	0.62	0.63

Chapter 4

Conclusions & Outlook

In this work we have studied InP/InGaP nanowires forming a tandem solar cell grown by the Vapor-Liquid Solid (VLS) method at Lund University (Sewden). We characterized the nanowires (NWs) using micro-Raman spectroscopy, micro-photoluminescence, tip-enhanced Raman spectroscopy (TERS), tip-enhanced photoluminescence (TEPL), and energy-dispersive X-ray (EDX) analysis to unveil their optical properties.

The micro-Raman results obtained along the NWs confirmed the zinc blende structure, while the wurtzite phase was not observed, although detailed analysis of this aspect requires x-ray diffraction experiments out of the scope of this work. The exposed face to the laser beam was (110). In this configuration, the TO modes are allowed and the LO modes are forbidden. The Raman selection rules were held in the InP cell, while in the InGaP cell the selection rules exhibit changes depending on the segment probed by the laser beam. In particular, in the tunnel junction, we found that the TO_1 mode decreased while the LO (LO_1 and LO_2) modes appeared, thus breaking the expected Raman selection rules. In the p^+-type side of the tunnel junction the frequency of the LO mode indicated that the concentration of In was $\approx 25\%$, which is lower than the one reported by the

growers. This smaller percentage of Indium is relevant since it yields InGaP alloys with an indirect bandgap, and thereby an expected quenching of the luminescence emission. Nevertheless, it is in agreement with EDX measurements, and also accounts for the absence of luminescence emission. Moreover, an additional peak appeared around 355 cm^{-1}, and it was assigned to an LO phonon hole plasmon coupled (LOPC) mode. Furthermore, we found a strong resonance in the p-InP/p^{+}InGaP region which produced an enhancement of the LOPC mode intensity. This enhancement is due to the dielectric mismatch, which produces the localization of the electromagnetic field, responsible for the high local Raman intensity in that region. Furthermore, the sharp electric field gradient associated with the localization of the electric field at the tunnel junction would be at the origin of the breakdown of the Raman selection rules, which hold for long order ranges, but fail for sharp gradients. The strong LOPC mode observed at the tunnel junction appears as a powerful method for characterizing the tunnel junctions, which is a crucial issue for the performance of many devices.

The photoluminescence data revealed an axial parasitic shell of InGaP deposited around the lower part of the NW, mostly on the InP cell. The presence of PL bands below the nominal bandgap of InGaP is assigned to the presence of defects, and to the parasitic InGaP layer grown laterally. The very weak emission was related to the fact that the InGaP composition is very close to the direct /indirect band-gap cross composition, and also to the high surface recombination velocity is detrimental to the luminescence emission. Tip-enhanced Raman spectroscopy and tip-enhanced photoluminescence with nanometric spatial resolution were used to complement the micro-PL and micro Raman measurements. Tip-enhanced Raman spectroscopy revealed the full spectrum of optical modes of InGaP, and the two modes of InP: LO and TO, because the Raman selection rules are different in both measurements due to the different electromagnetic field distribution and polarization in both cases. Additionally, tip-enhanced Raman spectroscopy revealed the parasitic

shell on InGaP in the InP cell, which was not detected in micro-Raman, confirming that TERS is more sensitive to surface signatures, because of the near field. Tip-enhanced Raman gives both higher lateral and in-depth spatial resolution than micro-Raman.

Tip-enhanced photoluminescence results were in agreement with the photoluminescence results. We observed bands in the tunnel junction region at 825 nm and < 925 that correspond to the emission from the parasitic InGaP layer. In the top cell, a broad band around 765 nm was observed in TEPL, similar to the one observed in micro photoluminescence. Therefore, this band should arise from the region close to the surface of the InP bottom cell. Finally, the chemical analysis made with EDX supports the composition estimation extracted from the Raman data.

This work will benefit from further research employing complementary techniques, such as the X-ray diffraction using a nanobeam and Synchrotron radiation, in order to ascertain the phases present in the InP/InGaP NW and either rule out or find traces of wurtzite structure. Further research on NWs with tailored doping, diameter, length, and different growth parameters will enrich this work and yield trends of use for improved fabrication of NW-based solar cells, the ultimate goal of this research.

Bibliography

[1] Lindsey, R.; Dahlman, L. Climate change: Global temperature. 2022; https://www.climate.gov/news-features/understanding-climate/climate-change-global-temperature#:~:text=Earth's$%$20temperature$%$20has$%$20risen$%$20by,based$%$20on$%$20NOAA's$%$20temperature$%$20data.

[2] Shukla, P. *et al. Climate Change and Land: an IPCC special report on climate change, desertification, land degradation, sustainable land management, food security, and greenhouse gas fluxes in terrestrial ecosystems*; 2010.

[3] The Sustainable Development Agenda - United Nations Sustainable Development. https://www.un.org/sustainabledevelopment/development-agenda/.

[4] Hannah Ritchie, M. R.; Rosado, P. Energy. *Our World in Data* **2020**, https://ourworldindata.org/energy.

[5] Louwen, A.; Van Sark, W.; Schropp, R.; Faaij, A. A cost roadmap for silicon heterojunction solar cells. *Solar Energy Materials and Solar Cells* **2016**, *147*, 295–314.

[6] Battaglia, C.; Cuevas, A.; De Wolf, S. High-efficiency crystalline silicon solar cells: status and perspectives. *Energy & Environmental Science* **2016**, *9*, 1552–1576.

[7] Fan, J. C. In *Energy, Resources and Environment*; Yuan, S., Ed.; Pergamon, 1982; pp 480–491.

[8] Day, J.; Senthilarasu, S.; Mallick, T. K. Improving spectral modification for applications in solar cells: A review. *Renewable Energy* **2019**, *132*, 186–205.

[9] Corkish, R. In *Encyclopedia of Energy*; Cleveland, C. J., Ed.; Elsevier: New York, 2004; pp 545–557.

[10] Nelson, C. A.; Monahan, N. R.; Zhu, X.-Y. Exceeding the Shockley–Queisser limit in solar energy conversion. *Energy & Environmental Science* **2013**, *6*, 3508–3519.

[11] Iles, P. A. In *Encyclopedia of Energy*; Cleveland, C. J., Ed.; Elsevier: New York, 2004; pp 25–33.

[12] Wang, K.; Cao, B.; Chen, J.; Zhou, W. In *Modeling, Characterization, and Production of Nanomaterials*; Tewary, V. K., Zhang, Y., Eds.; Woodhead Publishing Series in Electronic and Optical Materials; Woodhead Publishing, 2015; pp 115–144.

[13] Reine, M. In *Encyclopedia of Modern Optics*; Guenther, R. D., Ed.; Elsevier: Oxford, 2005; pp 392–402.

[14] Yu, Z. J.; Carpenter, J. V.; Holman, Z. C. Techno-economic viability of silicon-based tandem photovoltaic modules in the United States. *Nature Energy* **2018**, *3*, 747–753.

[15] Chen, Y.; Pistol, M.-E.; Anttu, N. Design for strong absorption in a nanowire array tandem solar cell. *Scientific reports* **2016**, *6*, 1–8.

[16] Mikkelsen, A.; Lundgren, E. Surface science of free standing semiconductor nanowires. *Surface science* **2013**, *607*, 97–105.

[17] Hyun, J. K.; Zhang, S. *Magnetic Nano-and Microwires*; Elsevier, 2020; pp 103–133.

[18] Otnes, G.; Borgström, M. T. Towards high efficiency nanowire solar cells. *Nano Today* **2017**, *12*, 31–45.

[19] Stern, E.; Vacic, A.; Reed, M. A. Semiconducting nanowire field-effect transistor biomolecular sensors. *IEEE Transactions on Electron Devices* **2008**, *55*, 3119–3130.

[20] Yang, P.; Yan, R.; Fardy, M. Semiconductor nanowire: what's next? *Nano letters* **2010**, *10*, 1529–1536.

[21] Imamura, G.; Kawashima, T.; Fujii, M.; Nishimura, C.; Saitoh, T.; Hayashi, S. Distribution of active impurities in single silicon nanowires. *Nano letters* **2008**, *8*, 2620–2624.

[22] Dasgupta, N. P.; Sun, J.; Liu, C.; Brittman, S.; Andrews, S. C.; Lim, J.; Gao, H.; Yan, R.; Yang, P. 25th anniversary article: semiconductor nanowires–synthesis, characterization, and applications. *Advanced materials* **2014**, *26*, 2137–2184.

[23] Jimenez, J.; Tomm, J. W. *Spectroscopic Analysis of Optoelectronic Semiconductors*; Springer International Publishing: Cham, 2016; pp 77–142.

[24] Birman, J. L.; Cummins, H. Z.; Rebane, K. K. *Light scattering in solids*; Springer, 1979.

[25] Pura, J. L. Espectroscopía Raman y Fotoluminiscencia. 2022.

[26] Horiba, What is Tip Enhanced Raman spectroscopy? 2018; `https://www.horiba.com/ind/scientific/technologies/afm-raman/what-is-tip-enhanced-raman-spectroscopy/`.

[27] Torres-Rivero, K.; Bastos-Arrieta, J.; Fiol, N.; Florido, A. Metal and metal oxide nanoparticles: An integrated perspective of the green synthesis methods by natural products and waste valorization: applications and challenges. *Comprehensive Analytical Chemistry* **2021**, *94*, 433–469.

[28] Raval, N.; Maheshwari, R.; Kalyane, D.; Youngren-Ortiz, S. R.; Chougule, M. B.; Tekade, R. K. *Basic fundamentals of drug delivery*; Elsevier, 2019; pp 369–400.

[29] Sinha, K.; Mascarenhas, A.; Kurtz, S. R.; Olson, J. Determination of free carrier concentration in n-GaInP alloy by Raman scattering. *Journal of applied physics* **1995**, *78*, 2515–2519.

[30] Lucovsky, G.; Brodsky, M.; Chen, M.; Chicotka, R.; Ward, A. Long-Wavelength Optical Phonons in Ga 1- x In x P. *Physical Review B* **1971**, *4*, 1945.

[31] Suzuki, T.; Gomyo, A.; Iijima, S.; Kobayashi, K.; Kawata, S.; Hino, I.; Yuasa, T. Band-gap energy anomaly and sublattice ordering in GaInP and AlGaInP grown by metalorganic vapor phase epitaxy. *Japanese journal of applied physics* **1988**, *27*, 2098.

[32] Zachau, M.; Masselink, W. Luminescence and Raman measurements of In y Ga1- y P (0.3< y< 0.5) grown by gas-source molecular beam epitaxy. *Applied physics letters* **1992**, *60*, 2098–2100.

[33] Jimenez, J.; Tomm, J. W. *Spectroscopic Analysis of Optoelectronic Semiconductors*; Springer International Publishing: Cham, 2016; pp 143–211.

[34] Pura, J.; Anaya, J.; Souto, J.; Prieto, A.; Rodríguez, A.; Rodríguez, T.; Periwal, P.; Baron, T.; Jiménez, J. Electromagnetic field enhancement effects in group IV semiconductor nanowires. A Raman spectroscopy approach. *Journal of Applied Physics* **2018**, *123*, 114302.

[35] Pages, O.; Renucci, M.; Briot, O.; Aulombard, R. Coupled LO–plasmon modes in semi-insulating GaAs of ZnSe/GaAs heterojunctions. *Journal of applied physics* **1996**, *80*, 1128–1135.

[36] Pura, J. L.; Anaya, J.; Souto, J.; Prieto, Á. C.; Rodríguez, A.; Rodríguez, T.; Jiménez, J. Local electric field enhancement at the heterojunction of Si/SiGe axially heterostructured nanowires under laser illumination. *Nanotechnology* **2016**, *27*, 455709.

[37] Pura, J. L.; Anaya, J.; Jiménez, J. About the interaction between a laser beam and group IV nanowires: A study of the electromagnetic field enhancement in homogeneous and heterostructured nanowires. *physica status solidi (a)* **2018**, *215*, 1800336.

[38] Takase, M.; Ajiki, H.; Mizumoto, Y.; Komeda, K.; Nara, M.; Nabika, H.; Yasuda, S.; Ishihara, H.; Murakoshi, K. Selection-rule breakdown in plasmon-induced electronic excitation of an isolated single-walled carbon nanotube. *Nature Photonics* **2013**, *7*, 550–554.

[39] Mergenthaler, K.; Anttu, N.; Vainorius, N.; Aghaeipour, M.; Lehmann, S.; Borgström, M.; Samuelson, L.; Pistol, M.-E. Anti-Stokes photoluminescence probing k-conservation and thermalization of minority carriers in degenerately doped semiconductors. *Nature communications* **2017**, *8*, 1–6.

[40] Yang, M.-J.; Yamaguchi, M.; Takamoto, T.; Ikeda, E.; Kurita, H.; Ohmori, M. Photoluminescence analysis of InGaP top cells for high-efficiency multi-junction solar cells. *Solar Energy Materials and Solar Cells* **1997**, *45*, 331–339.

[41] Meng, L.; Huang, T.; Wang, X.; Chen, S.; Yang, Z.; Ren, B. Gold-coated AFM tips for

tip-enhanced Raman spectroscopy: theoretical calculation and experimental demonstration. *Optics express* **2015**, *23*, 13804–13813.

Abbreviations

AFM Atomic Force Microscope ix, 8, 15, 16, 29, 31

EDX energy-dispersive X-ray 17, 34, 35, 37–39

FET Field Effect Transistor 5, 6

FWHM Full Width-Half Maximum xi, 23

InGaP indium gallium phosphide 9, 12, 13

InP indium phosphide 9, 12, 13

IPCC Intergovernmental Panel on Clima Change 1

NOAA National Oceanic and Atmospheric Administration 1

NW nanowire v, ix, xi, 5–9, 11–17, 20, 21, 23–39

PL photoluminescence 8, 14, 15, 17, 25, 28, 30, 32, 33

PNA peptide nuclei acid 7

SDG Sustainable Development Goal 2

SEM Scanning Electron Microscopy ix, 12, 13, 18, 34

TEPL tip-enhanced photoluminescence 7, 8, 32–34, 37, 39

TERS tip-enhanced Raman spectroscopy 7, 8, 15–17, 28–33, 37

UN United Nations 1, 2

VLS Vapor-Liquid Solid 11, 37